Syntheses, Structures, and Electrochemistry of the Defective ccp [Pt33(CO)38]2- and the bcc [Pt40(CO)40]6-
Molecular Nanoclusters

(Article begins on next page)

05 February 2025

Syntheses, Structures, and Electrochemistry of the Defective ccp [Pt$_{33}$(CO)$_{38}$]$^{2-}$ and the bcc [Pt$_{40}$(CO)$_{40}$]$^{6-}$ Molecular Nanoclusters

Enrico Cattabriga,[†] Iacopo Ciabatti,[†] Cristina Femoni,[†] Tiziana Funaioli,[*,‡] Maria Carmela Iapalucci,[†] and Stefano Zacchini[*,†]

[†]Dipartimento di Chimica Industriale "Toso Montanari", Università di Bologna, Viale Risorgimento 4, 40136 Bologna, Italy

[‡]Dipartimento di Chimica e Chimica Industriale, University of Pisa, Via Moruzzi 13, 56124 Pisa, Italy

ABSTRACT: The molecular [Pt$_{33}$(CO)$_{38}$]$^{2-}$ nanocluster was obtained from the thermal decomposition of $_{Na2}$[Pt$_{15}$(CO)$_{30}$] in methanol. The reaction of [Pt$_{19}$(CO)$_{22}$]$^{4-}$ with acids (1−2 equiv) affords the unstable [Pt$_{19}$(CO)$_{22}$]$^{3-}$ trianion, which evolves with time leading eventually to the [Pt$_{40}$(CO)$_{40}$]$^{6-}$ hexa-anion. The total structures of both nanoclusters were determined via single-crystal X-ray diffraction. [Pt$_{33}$(CO)$_{38}$]$^{2-}$ displays a defective *ccp* Pt$_{33}$ core and shows that localized deformations occur in correspondence of atomic defects to "repair" them. In contrast, [Pt$_{40}$(CO)$_{40}$]$^{6-}$ shows a *bcc* Pt$_{40}$ core and represents the largest Pt cluster with a body-centered structure. The rich electrochemistry of the two high-nuclearity platinum carbonyl clusters was studied by cyclic voltammetry and electrochemical in situ Fourier transform infrared spectroscopy. The redox changes of [Pt$_{33}$(CO)$_{38}$]$^{2-}$ show features of chemical reversibility and electrochemical quasi-reversibility, and the vibrational spectra in the CO stretching region of the nine redox forms of the cluster [Pt$_{33}$(CO)$_{38}$]^{n} (n = 0 to −4, −6 to −9) are reported. Almost all the redox processes exhibited by [Pt$_{40}$(CO)$_{40}$]$^{6-}$ are chemically and electrochemically reversible, and the eight oxidation states of [Pt$_{40}$(CO)$_{40}$] from −4 to −11 were spectroscopically characterized. The effect of the more regular *bcc* Pt-carbonyl cluster structure of [Pt$_{40}$(CO)$_{40}$]$^{6-}$ with
respect to that of the defective *ccp* Pt$_{33}$ core on the redox behavior is discussed.

1. INTRODUCTION

Platinum crystallites and nanoparticles dispersed in miscellaneous supports are widely employed in catalysis.[1−5] The sizes and (at the nanometric level) shape of the metal dispersion are of paramount importance to determine the activity and selectivity of the catalytic systems.[6−10] In addition, the presence of defects such as steps, kinks, adatoms, jogs, and surface vacancies, may considerably influence the performances of real catalytic materials compared to model systems.[11,12] Bulky metals and surfaces are rigid systems. Nonetheless, as their sizes decrease at the nanometric or sub-nanometric level, they become more deformable and strongly affected by the surface ligands.[13,14] Thus, at this length scale, ultrasmall metal crystallites and nanoparticles become comparable to large molecular clusters.[15−19] For instance, platinum carbonyl clusters have been claimed as models to understand the adsorption of carbon monoxide on small platinum surfaces and nanoparticles.[20,21]

In the case of homoleptic Pt-CO clusters, CO-rich clusters adopt one-dimensional trigonal prismatic structures as shown by Chini clusters [Pt$_{3n}$(CO)$_{6n}$]$^{2-}$ (n = 2−8), whereas more compact metal cores are present in CO-poorer species.[22−25] Thus, [Pt$_{38}$(CO)$_{44}$]$^{2-}$ and [Pt$_{24}$(CO)$_{30}$]$^{2-}$ possess *ccp* structures, [Pt$_{26}$(CO)$_{32}$]$^{2-}$ has a *hcp* core,[20,25,26] and [Pt$_{15}$(CO)$_{19}$]$^{4-}$ displays a very irregular body-centered cubic (*bcc*) metal cage,[27] whereas [Pt$_{19}$(CO)$_{22}$]$^{4-}$ contains a D$_{5h}$ pentagonal prismatic structure.[28] Icosahedral and bis-icosahedral structures have been, then, found in Pt-CO clusters decorated by Cd-halide moieties.[29] This should be contrasted with bulk Pt and Pt nanoparticles, which always adopt *ccp* structures. As a matter of fact, it seems that the structures of high-nuclearity metal clusters (or ultrasmall metal nanoparticles) cannot be simply related to their size, and thus, there is not a regular structure-size relationship.[18,20] Analogous conclusions can be obtained by analyzing the crystal structures of Au-thiolates nanoclusters. This is probably because, at these length scales, M-ligand interactions are as important as M−M ones.[30−35] Therefore, we might expect that, at these sizes, the introduction of defects in the metal cage of the cluster should lead to a rearrangement of its structure to "repair" these defects and minimize its total energy. This might have some relevance to heterogeneous catalysis with ultradispersed metals.

In addition, high-nuclearity platinum carbonyl clusters exhibit a rich redox chemistry: they undergo several reversible one-electron oxidation and reduction processes affording relatively stable species, with charges ranging from 0 to −8, and, in one case, as far as −10.[20,25] Infrared spectro-electrochemistry has been utilized to characterize the vibrational properties of these clusters as a function of the charge. The CO stretching frequencies of terminal and bridging ligands have been found to downshift in near-linear fashion, as the n charge of the clusters becomes more negative.[20,25] The electrochemical behavior of these high-nuclearity clusters may be related to their regular and stable metal cages, which can reversibly accept and release electrons without any major structural rearrangement.[18] In addition, as evidenced by IR spectro-electrochemical experiments, the fact that both terminal and bridging vCO bands shift with the charge of the cluster without changing, in most cases, their relative intensities, suggests that also the stereochemistry of the CO ligands is almost retained during the redox processes. Thus, it would be of interest to perform similar electrochemical and spectro-electroichemical studies on less regular and defective platinum clusters, to see if these structural features have some effects on their redox behavior.

Herein, we report the syntheses and total structures of the molecular [Pt$_{33}$(CO)$_{38}$]$^{2-}$ and [Pt$_{40}$(CO)$_{40}$]$^{6-}$ nanoclusters. The latter represents the first case of a high-nuclearity Pt carbonyl cluster adopting a *bcc* structure, whereas [Pt$_{33}$(CO)$_{38}$]$^{2-}$ displays a defective *ccp* structure. A detailed analysis of its structure shows that localized deformations

occur in correspondence of these atomic defects to "repair" them and stabilize the whole cluster. Both clusters show a rich redox activity, as evidenced by electrochemical and spectro-electrochemical studies. These redox processes are better defined in cyclic voltammetry for the more regular $[Pt_{40}(CO)_{40}]^{6-}$ nanocluster than the defective and distorted $[Pt_{33}(CO)_{38}]^{2-}$. Electrochemical in situ Fourier transform infrared (FTIR) spectroscopy allowed the characterization of nine and eight differently charged species of $[Pt_{33}(CO)_{38}]^{n}$ (n = 0 to −4, −6 to −9) and $[Pt_{40}(CO)_{40}]^{n}$ (n = −4 to −11), respectively.

2. RESULTS AND DISCUSSION

2.1. Synthesis and Structure of $[Pt_{33}(CO)_{38}]^{2-}$. The title compound has been obtained in moderate yields (ca. 23% based on Pt) after refluxing $Na_2[Pt_{15}(CO)]$ in CH_3OH and precipitated as $[NEt_4]^+$ salt. Its structure has been fully elucidated by X ray crystallography as its $[NEt_4]_2[Pt_{33}(CO)_{38}]\cdot THF$ salt (THF = tetrahydrofuran). These crystals show v_{CO} stretchings as solid in mineral oil mull at 2027(s) and 1792(w) cm^{-1}. They are soluble in polar organic solvents such as MeCN, where they display v_{CO} bands at 2030(s), 1830(m), and 1776(m) cm^{-1}.

Thermal decomposition of Chini clusters in miscellaneous solvents has been previously employed for the synthesis of other Pt carbonyl nanoclusters. Thus, $[Pt_{15}(CO)_{19}]^{4-}$ has been obtained after refluxing $[Pt_9(CO)_{18}]^{2-}$ in methanol in the presence of NaOH.[27] Conversely, the thermal decomposition of $[Pt_9(CO)_{18}]^{2-}$ as tetra-alkyl-ammonium salt in MeCN affords $[Pt_{19}(CO)_{22}]^{4-}$.[28] Finally, heating at reflux $[PPh_4]_2[Pt_{15}(CO)_{30}]$ in THF leads to a mixture of $[Pt_{24}(CO)_{30}]^{2-}$ and $[Pt_{26}(CO)_{32}]^{2-}$, which can be separated because of their different solubilities in organic solvents.[20,25,26]

The molecular structure of the $[Pt_{33}(CO)_{38}]^{2-}$ nanocluster (Figure 1) is composed of a defective Pt_{33} *ccp* metal core decorated by 38 CO ligands. The metal kernel of this cluster may be derived from the one of the previously reported $[Pt_{38}(CO)_{44}]^{2-}$ (Figure 2).[20,25,26] The latter is a truncated octahedron of frequency three composed of five layers along the (100) direction of the idealized *ccp* lattice, comprising 4, 9, 12, 9, and 4 Pt atoms, respectively (Figure 2c). The Pt_{38} kernel displays an almost perfect *ccp* structure with all the Pt−Pt contacts comprised in a very narrow range [2.745(3)− 2.9036(17) Å; average 2.820(18) Å]. A Pt_6 octahedron is fully embedded within the structure of $[Pt_{38}(CO)_{44}]^{2-}$. The Pt_{33} core of $[Pt_{33}(CO)_{38}]^{2-}$ is formally obtained after removing one of the two external Pt_4 layers and a further Pt-atom from the adjacent Pt_9 layer. Overall, the Pt_{33} framework is composed along (100) of four layers, comprising 4, 9, 12, and 8 atoms, respectively (Figure 2a). As a result of removing these five Pt atoms, one vertex of the Pt_6 octahedron, which was fully interstitial in $[Pt_{38}(CO)_{44}]^{2-}$, is now exposed on the surface of the cluster leaving only a square pyramidal Pt_5 fragment as fully interstitial. In view of its defective ccp structure, the Pt_{33} core of $[Pt_{33}(CO)_{38}]^{2-}$ displays significant distortions and deformations compared to an idealized Pt_{33} *ccp* structure (Figure 2b). First of all, the 121 Pt−Pt contacts of $[Pt_{33}(CO)_{38}]^{2-}$ are very spread [2.6589(16)−3.302(3) Å; average 2.822(16) Å]. The covalent and van der Waals radii of Pt are 1.36 and 1.72 Å, respectively.[36] Thus, the loosest Pt−Pt contacts displayed by this cluster are at the limit between bonding and nonbonding, even if below twice the van der Waals radius of Pt (3.44 Å). For comparison, (weak) Pt−Pt bonds up to ca. 3.34 Å have been detected in the solid-state structures of the $[Pt_{3n}(CO)_{6n}]^{2-}$ (n = 2−8) Chini clusters.[23,24]
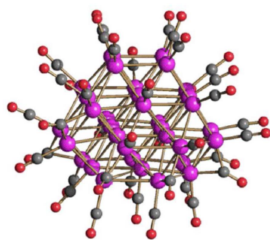

Figure 1. Molecular structure of $[Pt_{33}(CO)_{38}]^{2-}$ (purple, Pt; red, O; gray, C). Pt−Pt 2.6589(16)−3.302(3) Å; average 2.822(16) Å.

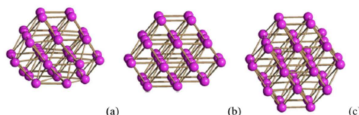**Figure 2.** View along (100) of (a) the Pt_{33} core of $[Pt_{33}(CO)_{38}]^{2-}$, (b) an idealized *ccp* Pt_{33} fragment, (c) the Pt_{38} core of $[Pt_{38}(CO)_{44}]^{2-}$.

A better insight on the deformations occurring in the Pt_{33} kernel of $[Pt_{33}(CO)_{38}]^{2-}$ may be obtained by drawing an idealized Pt_{33} *ccp* core with all the Pt−Pt contacts set equal to 2.82 Å, which is the average value found in the real cluster (Figure 2b). First of all, this idealized Pt_{33} *ccp* fragment displays 119 Pt−Pt contacts, and not 121 as in $[Pt_{33}(CO)_{38}]^{2-}$ (Figure 3). Moreover, a view along the (100) direction (Figure 4) indicates that major deformations occur close to the Pt_8 layer (layer 4), from which an atom is missing. Conversely, the Pt_4 and Pt_9 layers (layers 1 and 2) are almost not distorted and very close to the geometry displayed by the idealized Pt_{33} *ccp* fragment. Major deformations start in the Pt_{12} layer (layer 3), and then, layer 4 (Pt_8) completely departs from the idealized geometry. These deformations are needed to stabilize the otherwise high-energy defective (100) Pt_8 plane present in the idealized fragment (layer 4), which contains unsaturated five and six-coordinated (considering only the Pt−Pt bonds) Pt atoms. The above localized deformations increase the Pt−Pt connectivity of these atoms, lowering their energy and stabilizing the cluster. Otherwise, low Pt−Pt connected atoms are reminiscent of surface defects such as kinks and steps. Thus, it may be concluded that localized deformations occur in the Pt_{33} metal framework of $[Pt_{33}(CO)_{38}]^{2-}$ to repair the defects present in an idealized defective Pt_{33} ccp kernel.

$[Pt_{33}(CO)_{38}]^{2-}$ displays 38 CO ligands, 28 terminal and 10 edge bridging. It is noteworthy that it contains one ligand less than expected from the analogy with $[Pt_{38}(CO)_{44}]^{2-}$. In fact, $[Pt_{33}(CO)_{38}]^{2-}$ possesses 470 cluster valence electrons

(CVE) corresponding to 235 (6n + 7; n = number of metal atoms) cluster valence molecular orbitals (CVMO), whereas $[Pt_{33}(CO)_{38}]^{2-}$ possesses 408 CVE and 204 (6n + 6) CVMO. Thus, the addition of a further CO ligand to $[Pt_{33}(CO)_{38}]^{2-}$ would result in the same electron count (6n+ 7), but this is hampered on the basis of steric considerations.

We might speculate that, in the absence of the deformations of the Pt_{33} kernel, there would have been space for an additional CO ligand. Thus, the occurrence of these deformations is indicative of the fact that the cluster prefers to increase the number of Pt–Pt connectivities and reduce its surface available for CO coordination, in view of the higher total energy of the additional Pt–Pt interactions compared to that of the possible additional Pt-CO ones. Moreover, these deviations of the real structure from the idealized $_{ccp}$ model make the metal core of the cluster more spheroidal minimizing its surface.
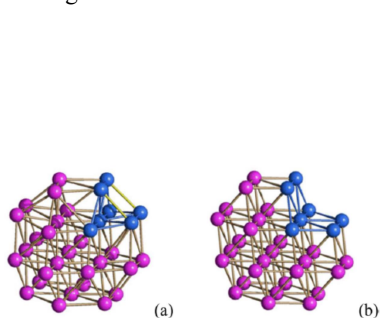

Figure 3. (a) View of the kink of the Pt_{33} core of $[Pt_{33}(CO)_{38}]^{2-}$, compared to (b) an idealized *ccp* Pt_{33} fragment. The Pt atoms of the kink are represented in blue; other Pt atoms are in purple. The two extra Pt–Pt bonds of (a) are represented in yellow; (a) 121 Pt–Pt bonds, (b) 119 Pt–Pt bonds. In this Figure, the view is rotated compared to Figures 1 and 2
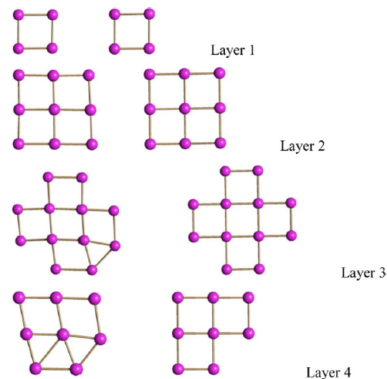

Figure 4. Four layers along (100) composing the Pt_{33} core of $[Pt_{33}(CO)_{38}]^{2-}$. (left) Real cluster. (right) Idealized *ccp* fragment. See for comparison Figure 2.

2.2. Synthesis and Structure of $[Pt_{40}(CO)_{40}]^{6-}$. It has been previously reported that the oxidation of $[Pt_{19}(CO)_{22}]^{4-}$ with a large excess of acid, via the H^+/H_2 redox couple, results in the larger *ccp* $[Pt_{38}(CO)_{44}]^{2-}$ nanocluster.[26] Conversely, its reaction with a stoichiometric amount of H^+ gives the isonuclear $[Pt_{19}(CO)_{22}]^{3-}$ trianion, which has been fully characterized via IR spectroscopy as well as electrochemical and spectro-electrochemical methods.[25] Nonetheless, its structure has not been yet determined, since it evolves with time to other species and does not survive to any workup procedure. Thus, to shed some light on the first step of the oxidation of $[Pt_{19}(CO)_{22}]^{4-}$ [v_{CO} 2005(s), 1799(ms) cm^{-1}], we performed its complete transformation into $[Pt_{19}(CO)_{22}]^{3-}$ [v_{CO} 2024(s), 1824(ms) cm^{-1}] with a slight excess of $HBF_4 \cdot Et_2O$ in MeCN solution. At the end of the reaction, the solution was filtered and layered with n-hexane and isopropyl ether resulting in crystals of $[NMe_3(CH_2Ph)]_5[NEt_4][Pt_{40}(CO)_{40}] \cdot 3MeCN$ suitable for X-ray analyses (yield 42% based on Pt). These crystals, once dissolved in MeCN, display v_{CO} bands [2027(s), 1831(m) cm^{-1}] significantly different from the starting solution of $[Pt_{19}(CO)_{22}]^{3-}$ (Figure S.3 in Supporting Information), confirming the different nature of the two species. Thus, we may conclude that $[Pt_{19}(CO)_{22}]^{3-}$ is not stable and, with time, evolves to give $[Pt_{40}(CO)_{40}]^{6-}$ (Scheme 1).

Scheme 1

$[Pt_{19}(CO)_{22}]^{4-} \xrightarrow{+H^+} [Pt_{19}(CO)_{22}]^{3-} \xrightarrow{time} [Pt_{40}(CO)_{40}]^{6-}$

The molecular structure of $[Pt_{40}(CO)_{40}]^{6-}$ (Figure 5) is composed of a Pt_{40} *bcc* metal core decorated by 40 CO ligands, 24 terminal and 16 edge bridging. It represents the first highnuclearity Pt nanocluster structurally characterized that adopts a *bcc* structure. Only the lower nuclearity species $[Pt_{15}(CO)_{16}]^{4-}$ displayed a very distorted *bcc* structure. As far as we are aware, there are no other examples of *bcc* structures in the chemistry of Pt molecular clusters, metal nanoparticles, or nanocrystals.
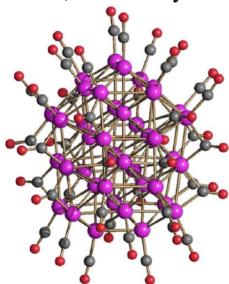

Figure 5. Molecular structure of $[Pt_{40}(CO)_{40}]^{6-}$ (purple, Pt; red, O; gray, C). Pt–Pt 2.6478(11)–3.364(2) Å; average 2.830(5) Å.

The 153 Pt–Pt contacts present in the bcc Pt_{40} core of $[Pt_{40}(CO)_{40}]^{6-}$ are comprised within a rather wide interval [2.6478(11)–3.364(2) Å; average 2.830(5) Å]. For comparison the covalent and van der Waals radii for Pt are 1.36 and

1.72 Å, respectively.[36] This makes the longest Pt−Pt contacts in the above cluster at the limit between bonding and nonbonding. The Pt_{40} core of $[Pt_{40}(CO)_{40}]^{6-}$ is compared in Figure 6 to an idealized *bcc* Pt_{40} fragment, in which the closest Pt−Pt contacts were set up identical to the average value found in the real cluster [2.83 Å]. It is noteworthy that the idealized *bcc* Pt_{40} fragment displays 168 Pt−Pt bonds, 15 more than the real cluster. The transformation from idealized *bcc* fragment to the real one includes expansions along [100] and [010] directions as well as significant compression along [001] direction, making the metal core of the cluster more spheroidal.
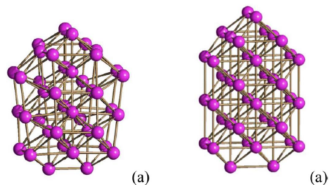

Figure 6. Pt_{40} metal core of $[Pt_{40}(CO)_{40}]^{6-}$ (a), and an idealized *bcc* Pt_{40} fragment with the same average Pt−Pt distances (b). (a) 153 Pt−Pt bonds, (b) 168 Pt−Pt bonds.

$[Pt_{40}(CO)_{40}]^{6-}$ possesses 486 CVE, which corresponds to 243 (6n + 3) CVMO. For comparison, $[Pt_{38}(CO)_{44}]^{2-}$ displays 470 CVE and 235 (6n + 7) CVMO, whereas $[Ni_{38}Pt_6(CO)_{48}]^{6-}$ possesses 542 CVE and 271 (6n + 7) CVMO; both clusters display *ccp* structures and a nuclearity comparable to $[Pt_{40}(CO)_{40}]^{6-}$. The largest metal carbonyl clusters possessing a *bcc* metal core, previous to this work, were $[H_{8-n}Rh_{22}(CO)_{35}]^{n-}$ (n = 4, 5),[37] $[Rh_{18}Pt_4(CO)_{35}]^{4-}$,[38] both with 6n + 6 CVMO, and $Pd_{23}(CO)_{20}(PEt_3)_8$ (6n + 5 CVMO).[39] Thus, $[Pt_{40}(CO)_{40}]^{6-}$ seems to be quite electronpoor. Within the structure of $[Pt_{40}(CO)_{40}]^{6-}$, there are eight Pt atoms fully interstitial, arranged as a snub disphenoid (ordodecadeltahedron; Johnson solid J_{84}), which has 12 triangular faces and D_{2d} symmetry (Figure 7).[40] It is also worthwhile to note that a number of the filled CVMOs in the obtained clusters reflects the availability of ligands, that is, the Pt/CO ratio in the corresponding precursors: compare $[Pt_{15}(CO)_{30}]^{2-}$ (Pt/CO = 0.5) for $[Pt_{33}(CO)_{38}]^{2-}$ (6n + 6 CVMO) with $[Pt_{19}(CO)_{22}]^{3-}$ (Pt/CO = 0.86) for $[Pt_{40}(CO)_{40}]^{6-}$ (6n + 3 CVMO).
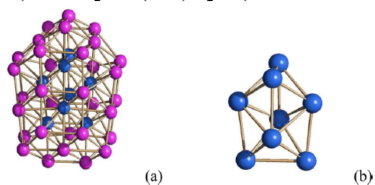

Figure 7. Pt_{40} metal core of $[Pt_{40}(CO)_{40}]^{6-}$ with evidenced in blue the eight fully interstitial Pt (a), and the resulting snub disphenoid (b).

Finally, even if the kinds of deviations occurring in $[Pt_{33}(CO)_{38}]^{2-}$ and $[Pt_{40}(CO)_{40}]^{6-}$ compared to idealized *ccp* and *bcc* models, respectively, are different, the common rationale for these deviations is to make the real geometries more spheroidal. With a given n, a higher sphericity generally results in a smaller surface area with a smaller number of ligands. Thus, regardless of electron sufficiency (6n + 6 CVMO in $[Pt_{33}(CO)_{38}]^{2-}$) or deficiency (6n + 3 CVMO in $[Pt_{40}(CO)_{40}]^{6-}$) both structures minimize their surface.

2.3. Electrochemistry and Infrared Spectro-Electrochemistry of $[Pt_{33}(CO)_{38}]^{2-}$. The $[Pt_{33}(CO)_{38}]^{2-}$ dianion exhibits a rich redox activity (Figure 8), as previously found for other high-nuclearity Pt carbonyl clusters.[20,25] Its voltammetric profile at a Pt electrode displays several (ill-defined) processes, among which three appear as oxidations and four as reductions, showing some features of electrochemical and chemical reversibility.[41] The formal electrode potentials for the observed electron transfers are compiled in Table 1. If compared with the cyclic voltammetry of the structurally more regular $[Pt_{19}(CO)_{22}]^{4-}$, $[Pt_{24}(CO)_{30}]^{2-}$, $[Pt_{26}(CO)_{32}]^{2-}$, and $[Pt_{38}(CO)_{44}]^{2-}$,[20,25] which show a sequence of close-spaced pairs of reversible one-electron processes, the behavior of $[Pt_{33}(CO)_{38}]^{2-}$ appears quite different, in that the waves are unlike in shape and separation and have variable height. The only common feature of the cyclic voltammetries of all these clusters is an intense peak, assigned to adsorption of the electrogenerated species,[25] observed in the backscan after the most anodic process. Even with the aid of hydrodynamic techniques, it was not possible to establish the relative number of electrons exchanged in each single step.

Table 1. Formal Electrode Potentials[a] and Peak-to-Peak Separations (mV) for the Redox Processes Exhibited in the Cyclic Voltammetry of $[Pt_{33}(CO)_{38}]^{2-}$ in MeCN Solution

	oxidation processes					reduction processes						
$E°_1$	$E°_2$	$\Delta E_p{}^b$	$E°_3$	$\Delta E_p{}^b$	$E°_4$	$\Delta E_p{}^b$	$E°_5$	$\Delta E_p{}^b$	$E°_6$	$\Delta E_p{}^b$	$E°_7$
+0.12[c]	−0.15	95	−0.43	90	−0.87	90	−1.14	90	−1.72	136	−2.07
(+0.51)	(0.24)		(−0.04)		(−0.48)		(−0.75)		(−1.33)		(−1.68)

[a]Volts vs $FeCp_2$ and (in brackets) vs SCE. [b]Measured at 0.1 V s⁻¹. [c]Peak potential value for irreversible processes.

The electrochemical redox processes of the dianion $[Pt_{33}(CO)_{38}]^{2-}$ were studied also by electrochemical in situ FTIR in an optically transparent thin-layer electrochemical (OTTLE) cell. The potential of the working electrode was swept

between +0.3 and −2.7 V (vs FeCp2) at the scan rate of 0.5 mV s−1, and a sequence of vibrational spectra in the CO stretching region was collected at constant time intervals. The profile of the curve current versus potential obtained during the slow scan of the potential (Figure 8d) points out the presence of seven major redox processes, four reductions, and three oxidations, in accord to cyclic voltammetry. Two further reductions of the cluster, respectively, at −2.37 and −2.70 V, are hidden in Figure 8d by the solvent discharge, but their presence in the spectro-electrochemical experiments is evidenced by the analysis of the IR spectra of the electrogenerated species (see below). Moreover, on lowering the applied potential, a gradual and continuum shift to lower wavenumbers of the terminal and bridging v^t_{CO} bands is observed in the IR spectro-electrochemical experiments. This process is perfectly reversed by increasing the potential.

At first, we verified that the potential can be cycled between +0.3 and −2.4 V without decomposition of the electrogenerated species, and that the IR spectrum of the starting cluster $[Pt_{33}(CO)_{38}]^{2-}$ can be obtained when the working electrode potential is returned to the initial value (−0.7 V). When the working electrode potential was driven down to −2.7 V, one further reduction of the cluster, overlapping the solvent discharge, is pointed out by the IR spectral changes, and is followed by a relatively fast transformation into a species that does not regenerate the starting spectrum of the dianion in the reverse oxidation backscan.
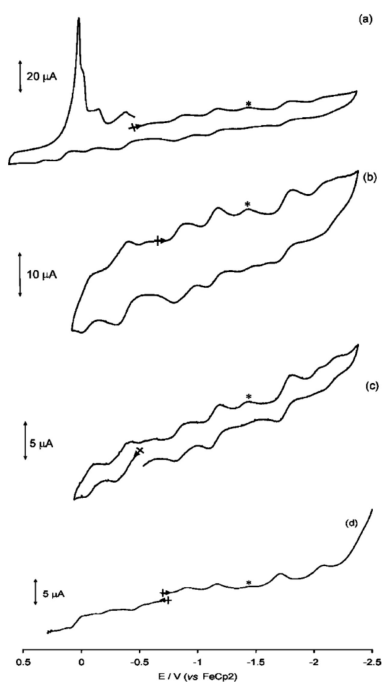
Figure 8. Cyclic voltammograms recorded at a platinum electrode in MeCN solutions of $[Pt_{33}(CO)_{38}]^{2-}$. $[N^nBu_4][PF_6]$ (0.1 mol dm^{-3}) as supporting electrolyte. (a, b) Scan rate: 0.1 V s^{-1}; (c) scan rate: 0.02 V s^{-1}; (d) profile current vs E obtained in the OTTLE cell on the same solution varying the potential between +0.3 and −2.7 V at a scan rate = 0.5 mV s^{-1}. (*) Impurity (see Supporting Information Figure S.6).

During the oxidation at the most anodic potential (+0.30 V), we observed, instead of the expected upshift, a gradual decrease of all the IR absorptions attributable to CO ligands, and an inspection of the IR cell at the microscope revealed that the Pt grid working electrode was completely covered by a needlelike precipitate that, on lowering the potential to 0.0 V, completely redissolved, restoring in solution the IR bands of the cluster.

By the comparison between the sequences of IR spectra and the profile of the i/E curve, we were able to separate the spectra in eight groups, each of them attributable to an electron exchange (see Supporting Information Figures S.4−S.10 for all the spectral sequences). In this way, the IR spectra (in the v_{CO} region) of the nine redox states of the cluster were selected (Table 2 and Figure 9).

Table 2. Infrared Stretching Frequencies (cm^{-1}) of Terminal (v^t_{CO}) and Bridging (v^b_{CO}) Carbonyl Groups for $[Pt_{33}(CO)_{38}]^n$ in MeCN as a Function of the Cluster Charge n

cluster charge n	v^t_{CO}	v^b_{CO}
0	2056	1862, 1804
−1	2044	1847, 1793
−2	2030	1830, 1776
−3	2016	1815, 1760
−4	2009(sh), 2002	1799, 1741
−6	1974	1788, 1774
−7	1980(sh), 1955, 1937(sh)	1783, 1774(sh), 1740
−8	1967(sh), 1937	1769
−9	1950(sh), 1920, 1898(sh)	1752
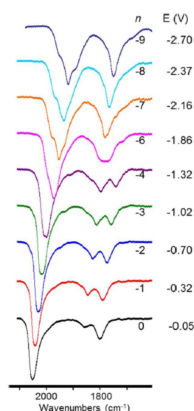
Figure 9. Selected infrared spectra of $[Pt_{33}(CO)_{38}]^n$ as a function of the cluster charge n, and of the potential E, in MeCN containing 0.1 M $[NBu_4][PF_6]$. The absorptions of the solvent and the supporting electrolyte have been subtracted.

Well-defined isosbestic points are observable for each process, at least for the bridging carbonyl absorptions, as shown, for example, in Figure 10 for the first oxidation and the first reduction. Conversely, terminal carbonyl absorptions shift to higher or lower frequencies, depending on the sweep potential, in most cases without a well-defined isosbestic point. As illustrated in Figure 9, the ν_{CO} bands change shape and intensity by changing the charge of the cluster. In particular, ν^t_{CO} bands are narrower for the most oxidized species and broaden upon reduction, until becoming, for the most reduced clusters, a band with two shoulders. Conversely, the two ν^b_{CO} bands change their intensity on changing the charge of the cluster and coalesce to a single absorption in the more reduced species.

Moreover, the relative intensity of ν^t_{CO} and ν^b_{CO} bands varies with the redox state of the cluster. In particular, the ν^b_{CO} bands become more and more intense as the negative charge increases, according to the general observation that an increase of the negative charge of a cluster leads to an increased tendency for CO ligands to display a bridging coordination mode.[42] All these observations, together with the complete chemical reversibility of the redox processes occurring between +0.3 and −2.4 V, point out that the structure of $[Pt_{33}(CO)_{38}]^n$ is stable with a variable number of electrons, but some structural changes, especially regarding the stereochemistry of the CO ligands, occur on the same time scale of the spectroelectrochemical experiment. This can be inferred also from the ΔE_p values measured in the cyclic voltammetric experiments, where values higher than 90 mV indicate the quasi-reversibility of the electron transfers.
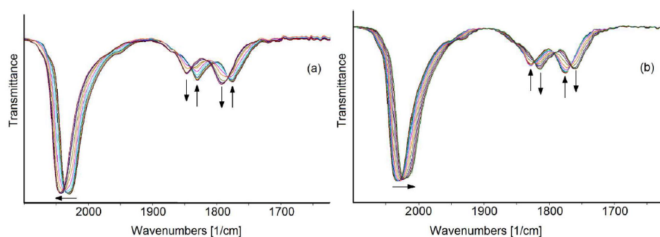
Figure 10. IR spectral changes recorded in an OTTLE cell during the progressive one-electron (a) first oxidation (E from −0.70 to −0.32 V), and (b) first reduction (E from −0.70 to −1.02 V) of $[Pt_{33}(CO)_{38}]^{2-}$ in MeCN solution. $[N^nBu_4][PF_6]$ (0.1 mol dm^{-3}) was the supporting electrolyte. The absorptions of the solvent and the supporting electrolyte were subtracted.

The two most cathodic reduction processes of the cluster are masked, in the voltammetric profile of Figure 8d, by the solvent discharge, but they are well-documented by the spectroelectrochemical experiments (see Figures S.9 and S.10 in Supporting Information). Gas evolution and fast modification of the spectra, at potential beyond −2.7 V, pointed out decomposition of the electrogenerated cluster.

Finally, by the comparison of the stretching frequencies of terminal CO ligands belonging to the reversible redox states of the cluster, we observed for all processes, except the reduction at −1.72 V, a near-uniform shift of 14 cm^{-1}, indicating one-electron transfers.[20,25] Similarly, the decrease of the ν^t_{CO} by 28 cm^{-1}, associated with the reduction at −1.72 V, was assigned to a two-electron step (Table 2). This is supported also by the greater height of the reduction wave in the voltammetric profile of Figure 8d. Concerning the most anodic reversible process at +0.3 V, the insolubility of the electrogenerated product precluded to obtain its IR spectrum, but the height of the voltammetric wave indicates that two or more electrons are involved in this electron exchange, giving the stable cationic cluster $[Pt_{33}(CO)_{38}]^{+m}$.

On the basis of the spectro-electrochemical experiments, by sweeping the potential of the working electrode between +0.3 and −2.7 V (vs FeCp$_2$) in 0.1 M $[NBu_4][PF_6]$/MeCN, we identified eight resolvable, long-lived, oxidation states of the cluster, that is, $[Pt_{33}(CO)_{38}]^{0/1-/2-/3-/4-/6-/7-/8-}$. Moreover, we were able to acquire the IR spectrum of the unstable anionic cluster $[Pt_{33}(CO)_{38}]^{9-}$, while the formation of the stable cation $[Pt_{33}(CO)_{38}]^{+m}$ was inferred from the reversible precipitation and dissolution of a solid depending on the applied potential.

2.4. Electrochemistry and Infrared Spectro-Electrochemistry of $[Pt_{40}(CO)_{40}]^{6-}$. As shown in Figure 11, the $[Pt_{40}(CO)_{40}]^{6-}$ hexa-anion exhibits a rich redox activity. Its voltammetric profile at a Pt electrode displays eight welldefined and close-spaced processes, among which four appear as oxidations and four as reductions, showing features of electrochemical and chemical reversibility, with the exception of the most anodic step, which is affected by precipitation of the electrogenerated species. The formal electrode potentials for the observed electron transfers are compiled in Table 3. The voltammetric profile appears more regular than that of $[Pt_{33}(CO)_{38}]^{2-}$, and it is reminiscent of that of $[Pt_{19}(CO)_{22}]^{4-}$, $[Pt_{24}(CO)_{30}]^{2-}$, $[Pt_{26}(CO)_{32}]^{2-}$, and $[Pt_{38}(CO)_{44}]^{2-}$.[20,25]

Figure 11. Cyclic voltammograms recorded at a platinum electrode in MeCN solutions of $[Pt_{40}(CO)_{40}]^{6-}$. $[N^nBu_4][PF_6]$ (0.1 mol dm^{-3}) as supporting electrolyte; scan rate: 0.1 V s^{-1}.

Table 3. Formal Electrode Potentials[a] and Peak-to-Peak Separations (mV) for the Redox Processes Exhibited in MeCN Solution by $[Pt_{40}(CO)_{40}]^{6-}$

	oxidation processes							reduction processes							
$E°_1$	$E°_2$	ΔE_p[b]	$E°_3$	ΔE_p[b]	$E°_4$	ΔE_p[b]	$E°_5$	ΔE_p[b]	$E°_6$	ΔE_p[b]	$E°_7$	ΔE_p[b]	$E°_8$	ΔE_p[b]
+0.11[c] (+0.50)	−0.18 (0.21)		−0.54 (−0.15)	70	−0.79 (−0.40)	70	−1.26 (−0.87)	80	−1.50 (−1.11)	90	−1.83 (−1.44)	80	−2.07 (−1.68)	90

[a]Volts vs FeCp$_2$ and (in brackets) vs SCE. [b]Measured at 0.1 V s^{-1}. [c]Peak potential value for irreversible processes.

The IR spectro-electrochemical analysis of the v_{CO} frequencies accompanying the redox changes of $[Pt_{40}(CO)_{40}]^{6-}$ was performed changing the potential of the working electrode of an OTTLE cell between −0.2 and −2.4 V (vs FeCp$_2$) at the scan rate of 0.5 mV s$_{-1}$. Also in this case we verified that the potential can be cycled between −0.2 and −2.4 V without decomposition of the electrogenerated species and that the IR spectrum of the starting cluster $[Pt_{40}(CO)_{40}]^{6-}$ can be restored when the working electrode potential is returned to the initial value of −1.0 V.

As illustrated in Figure 12 for the reduction step $[Pt_{40}(CO)_{40}]^{6-/7-}$, both the v^t_{CO} and v^b_{CO} bands are shifted toward lower wavenumbers as the electrode potential is lowered, and well-defined isosbestic points appear for both the bands, indicating the relative stability of the electrogenerated species. A similar trend is observed for all the reduction steps and the first oxidation process of the cluster $[Pt_{40}(CO)_{40}]^{6-}$ (see Supporting Information Figures S.11−S.15 for the spectral sequences of all the redox changes). This points out an electrochemical reversibility of the redox changes greater than $[Pt_{33}(CO)_{38}]^{6-}$, as showed also by the lower ΔE_P values measured in the cyclic voltammetric experiments.

Accordingly, during the first four reductions and the first oxidation, the v_{CO} bands maintain their original aspect and relative intensity, suggesting that, not only the metal kernel of $[Pt_{40}(CO)_{40}]^{6-}$ is stable with a variable charge but also the stereochemistry of the CO ligands remains almost unchanged. The spectro-electrochemical experiments allowed the identification of a further reduction process, hidden under the solvent discharge in the cyclic voltammetry, whose reduced product possesses a limited stability in the time scale of the spectroelectrochemical experiment.

Concerning the oxidation steps, three reversible processes are present in the cyclovoltammetric profile of Figure 11, while the intense peak in the forward cycle following the fourth oxidation indicates the precipitation at the electrode surface of the electrogenerated species. On this basis, the results of the IR spectro-electrochemical experiments appear different, at least for the second and subsequent oxidation steps. As shown in Figure 13 for the second oxidation step, when the potential of the working electrode is increased from −0.64 to −0.46 V, the expected upshift of v^t_{CO} (from 2039 to 2052 cm^{-1}) is accompanied by a modification of the intensity and the shape of the IR absorptions in the v^b_{CO} region. In particular, a weak band at 1856 and a medium intensity absorption at 1800 cm^{-1} appear instead of a single v^b_{CO} band at higher frequencies with respect to the 1845 cm^{-1} band displayed by $[Pt_{40}(CO)_{40}]^{5-}$. The process is completely reversible, and the IR spectrum of $[Pt_{40}(CO)_{40}]^{5-}$ is restored after electroreduction of $[Pt_{40}(CO)_{40}]^{4-}$. This may indicate that the formation of the tetra-anion is accompanied by a slight change of the stereochemistry of the CO ligands.[20b]
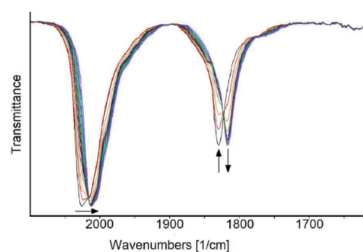
Figure 12. IR spectral changes recorded in an OTTLE cell during the progressive one-electron first reduction of $[Pt_{40}(CO)_{40}]^{6-}$ in MeCN solution (E from -1.00 to -1.40 V). $[N^nBu_4][PF_6]$ (0.1 mol dm^{-3}) as the supporting electrolyte. The absorptions of the solvent and the supporting electrolyte were subtracted.

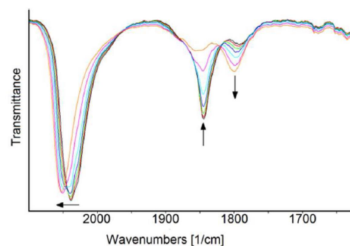**Figure 13.** IR spectral changes recorded in an OTTLE cell as the potential of an MeCN solution of $[Pt_{40}(CO)_{40}]^{6-}$ is increased anodically from -0.64 to -0.46 V, corresponding to the second oxidation step. $[N^nBu_4][PF_6]$ (0.1 mol dm^{-3}) as the supporting electrolyte. The absorptions of the solvent and the supporting electrolyte were subtracted.

By further increasing the potential from -0.46 to -0.28 V, corresponding to the third oxidation step (see Supporting Information Figure S.16), all the IR carbonyl bands gradually decrease their intensity suggesting, as in the case of $[Pt_{33}(CO)_{38}]^{2-}$, the precipitation of the electrogenerated species. Also in this case the process is completely reversible, and the IR absorptions of the starting cluster can be restored on lowering the potential to -1.0 V. Thus, the spectro-electrochemistry confirms the presence of stable oxidized species. Nonetheless, due to the different time scale of the cyclovoltammetric and spectro-electrochemical experiments, the precipitation follows the third oxidation during spectroelectrochemistry, whereas it occurs after the fourth oxidation in the CV experiment.

The stretching frequencies of terminal (v^t_{CO}) and bridging (v^b_{CO}) carbonyl groups of $[Pt_{40}(CO)_{40}]^n$ are reported in Table 4. The near-uniform shift of 12 cm^{-1}, observed for terminal CO, and 17 cm^{-1} for bridging CO, indicates that all the steps are one-electron transfer. The IR spectra in the CO stretching region of the clusters $[Pt_{40}(CO)_{40}]^n$ with the assigned charge n, together with the potential values to which each species is stable, are shown in Figure 14.
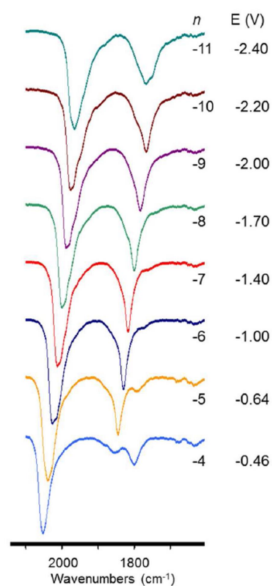

Figure 14. Selected infrared spectra of $[Pt_{40}(CO)_{40}]^n$ as a function of the cluster charge n, and of the potential E, in MeCN containing 0.1 M $[NBu_4][PF_6]$. The absorptions of the solvent and the supporting electrolyte were subtracted.

Table 4. Infrared Stretching Frequencies (cm^{-1}) of Terminal (ν^t_{CO}) and Bridging (ν^b_{CO}) Carbonyl Groups for $[Pt_{40}(CO)_{40}]^n$ in MeCN as a Function of the Cluster Charge n

cluster charge n	ν^t_{CO}	ν^b_{CO}
-4	2051	1856, 1799
-5	2039	1845
-6	2027	1831
-7	2012	1817
-8	2000	1800
-9	1988	1783
-10	1976	1767
-11	1966	1767, 1752(sh)

Overall, the combined study of the electrochemistry and *in situ* IR spectro-electrochemistry of $[Pt_{40}(CO)_{40}]^{6-}$ allowed the identification of nine redox processes (four oxidations and five reductions). These correspond to 10 possible oxidation states of the $[Pt_{40}(CO)_{40}]^{n-}$ species (n = 2–11). While the complete sequence of the four oxidation steps was observed only by cyclic voltammetry, the reduction process $[Pt_{40}(CO)_{40}]^{10-/11-}$, masked by the solvent discharge in cyclic voltammetry, was pointed out by the spectro-electrochemical experiments. These allowed the acquisition of the IR spectra of the seven long-lived oxidation states, that is, $[Pt_{40}(CO)_{40}]^{4-/5-/6-/7-/8-/9-/10-}$, and of the instable $[Pt_{40}(CO)_{40}]^{11-}$ cluster. Moreover, the spectroelectrochemical experiments demonstrated the stability of the more oxidized insoluble species, observed by the cyclic voltammetry.

3. CONCLUSIONS

The syntheses, total structures, and electrochemical behavior of the molecular $[Pt_{33}(CO)_{38}]^{2-}$ and $[Pt_{40}(CO)_{40}]^{6-}$ nanoclusters have been reported. The former displays a defective *ccp* structure formally originating after elimination of five Pt atoms from the regular *ccp* $[Pt_{38}(CO)_{44}]^{2-}$ cluster. Localized deformations occur in $[Pt_{33}(CO)_{38}]^{2-}$ to repair its atomic defects. Conversely, $[Pt_{40}(CO)_{40}]^{6-}$ represents the largest Pt cluster with a body-centered structure. A *bcc* structure has been recently observed also for $Au_{38}S_2(SR)_{20}$ (R = $C_{10}H_{25}$) in striking contrast to the *fcc* and other structures reported so far for gold nanoclusters.[31a] It is noteworthy that molecular platinum carbonyl clusters with nuclearities ranging from 19 to 40 display D$_{5h}$ pentagonal prismatic, *ccp, hcp,* or *bcc* structures without a clear structure-size relationship confirming previous findings.[18,20] As pointed out in the Introduction, this seems to be a general feature common to large molecular clusters and ultrasmall metal nanoparticles.

As found for other high-nuclearity platinum carbonyl clusters, both $[Pt_{33}(CO)_{38}]^{2-}$ and $[Pt_{40}(CO)_{40}]^{6-}$ display a rich electrochemistry, as shown by cyclic voltammetry and IR spectro-electrochemistry. Interestingly, in the case of the deformed and defective $[Pt_{33}(CO)_{38}]^{2-}$, its redox changes show features of chemical reversibility and electrochemical quasi-reversibility, whereas almost all the redox processes exhibited by the more regular $[Pt_{40}(CO)_{40}]^{6-}$ are chemically and electrochemically reversible. Similarly, $[Pt_{38}(CO)_{44}]^{2-}$, which displays an almost perfect *ccp* structure, shows also chemically and electrochemically reversible redox processes. This suggests that there might be some relationships between the structures and redox behavior of these large Pt carbonyl nanoclusters. It seems that electrons can be added/removed from more regular clusters, such as $[Pt_{40}(CO)_{40}]^{6-}$ and $[Pt_{38}(CO)_{44}]^{2-}$, without significantly altering their structures. Conversely, in the case of the deformed and defective $[Pt_{33}(CO)_{38}]^{2-}$, the chemical reversibility and electrochemical quasi-reversibility of its redox processes might indicate that some structural rearrangements involving the metal core and/or the stereochemistry of the CO ligands occur upon the addition/removal of electrons. These results suggest that atomic defects and geometrical deformations, as well as M−M and M−ligand interactions, have structural and electronic relevance in ultrasmall metal aggregates.

Finally, the fact that these molecular Pt nanoclusters display several redox states separated by relatively small $\Delta E°$ indicates that they possess a highest occupied molecular orbital−lowest unoccupied molecular orbital frontier region in which more orbitals weakly antibonding or nonbonding can be populated or depopulated without great effects on the metal framework stability. Overall, these findings confirm that high-nuclearity metal carbonyl clusters may behave as molecular nanocapacitors and electron sinks.[18,22,43]

4. EXPERIMENTAL SECTION

4.1. General Experimental Procedures. All reactions and sample manipulations were performed using standard Schlenk techniques under nitrogen and in dried solvents. All the reagents were commercial products (Aldrich) of the highest purity available and used as received except $[NMe_3(CH_2Ph)]_4[Pt_{19}(CO)_{22}]$, which was prepared according to literature methods.[28] Analyses of Pt were performed by atomic absorption on a Pye-Unicam instrument. Analyses of C, H, and N were obtained with a Thermo Quest Flash EA 1112NC instrument. IR spectra were recorded on a PerkinElmer Spectrum One interferometer in CaF_2 cells. Structure drawings were performed with SCHAKAL99.[44]

4.2. Synthesis of $[NEt_4]_2[Pt_{33}(CO)_{38}]\cdot THF$. $Na_2[PtCl_6]\cdot 6H_2O$ (1.80 g, 3.95 mmol) and $CH_3COONa\cdot 3H_2O$ (1.92 g, 14.1 mmol) were dissolved in methanol (30 mL) and stirred under a CO atmosphere overnight, resulting in the formation of a silky brown suspension of $Na_2[Pt_{3n}(CO)_{6n}]$ (n ≈ 10). A methanol solution of NaOH was then added dropwise under a CO atmosphere over 1 h until a green solution of $Na_2[Pt_{15}(CO)_{30}]$ was formed as confirmed by IR monitoring. The solution was refluxed under nitrogen for 3 h, turning from green to brown, and concomitantly the starting $Na_2[Pt_{15}(CO)_{30}]$ completely disappeared as shown by IR spectroscopy in the ν_{CO} region. The reaction mixture was precipitated by addition of a saturated solution of $[Et_4N]Br$ in water, and the solid was recovered by filtration under nitrogen, washed with water (40 mL) and THF (20 mL), and extracted with acetone (10 mL). The acetone solution, after filtration, was diluted with THF (10 mL), and crystals suitable for Xray analysis of $[NEt_4]_2[Pt_{33}(CO)_{38}]\cdot THF$ were obtained by layering n-hexane (40 mL; yield 0.22 g, 23% based on Pt).
$C_{58}H_{48}N_2O_{39}Pt_{33}$ (7834.95): calcd. (%): C 8.89, H 0.62, N 0.36, Pt 82.17; found: C 9.08, H 0.81, N 0.22, Pt 81.98. IR (mineral oil, 293 K) ν_{CO}: 2027(s), 1792(w) cm^{-1}. IR (acetone, 293 K) ν_{CO}: 2039(s), 1850(w) cm–1. IR (MeCN, 293 K) ν_{CO}: 2030(s), 1830(m), 1776(m) cm^{-1}.

4.3. Synthesis of $[NMe_3(CH_2Ph)]_5[NEt_4][Pt_{40}(CO)_{40}]\cdot 3MeCN$. $HBF_4\cdot Et_2O$ (40 μL, 0.291 mmol) was added to a solution of $[NMe_3(CH_2Ph)]_4[Pt_{19}(CO)_{22}]$ (0.69 g, 0.141 mmol) and $[Et_4N]Br$ (50 mg, 0.239 mmol) in MeCN (20 mL). The reaction was monitored by IR spectroscopy, and the addition of acid was stopped when $[Pt_{19}(CO)_{22}]^{4-}$ [ν_{CO} 2005(s), 1799(ms) cm^{-1}] was completely converted into $[Pt_{19}(CO)_{22}]^{3-}$ [ν_{CO} 2024(s), 1824(ms) cm^{-1}]. The resulting solution was filtered and layered with n-hexane (2 mL) and isopropyl ether (40 mL) resulting in crystals of $[NMe_3(CH_2Ph)]_5[NEt_4][Pt_{40}(CO)_{40}]\cdot 3MeCN$ suitable for X-ray analyses (yield 0.28 g, 42% based on Pt).
$C_{104}H_{109}N_9O_{40}Pt_{40}$ (9928.60): calcd. (%): C 12.58, H 1.11, N 1.27, Pt 78.60; found: C 12.24, H 1.36, N 1.51, Pt 78.92. IR (mineral oil, 293 K) ν_{CO}: 2014(s), 1820(w), 1793(w) cm^{-1}. IR (MeCN, 293 K) ν_{CO}: 2027(s), 1831(m) cm^{-1}. IR (dimethylformamide, 293 K) ν_{CO}: 2020(s), 1833(m) cm^{-1}.
The addition of $[Et_4N]Br$ was required to facilitate the crystallization. In the absence of $[Et_4N]Br$, the outcome of the reaction was exactly the same, but we could not obtain crystals suitable for X-ray analyses.

4.4. X-ray Crystallographic Study. Crystal data and collection details for $[NEt_4]_2[Pt_{33}(CO)_{38}]\cdot THF$ and $[NMe_3(CH_2Ph)]_5[NEt_4][Pt_{40}(CO)_{40}]\cdot 3MeCN$ are reported in Table 5. The diffraction experiments were performed on a Bruker APEX II diffractometer equipped with a CCD detector using Mo Kα radiation. Data were corrected for Lorentz polarization and absorption effects (empirical absorption correction SADABS).[45] Structures were solved by direct methods and refined by full-matrix least-squares based on all data using F_2.[46] Hydrogen atoms were fixed at calculated positions and refined by a riding model. All non-hydrogen atoms were refined with anisotropic displacement parameters, unless otherwise stated. Both structures present A and B

alerts due to high values for the residual electron density. These maxima are located close to the Pt atoms, and they are series termination errors, which are common with heavy atoms such as Pt, especially in the case of high-nuclearity clusters.

[NEt4]2[Pt33(CO)38]·THF. The asymmetric unit of the unit cell contains one cluster anion, two [NEt4]$^+$ cations, and one THF molecule (all located on general positions). One [NEt4]$^+$ cation is disordered over two independent positions, which have been refined isotropically using one occupancy parameter per disordered group. Because of partial disorder and the contemporary presence of several heavy atoms together with lighter C, O, and N atoms, some restraints were employed during the refinement. Thus, the C and O atoms of the CO ligands of the cluster anion, and the C and N atoms of the anisotropic [NEt4]$^+$ cation were restrained to isotropic behaviour (ISOR command in SHELXL, s.u. 0.01). The [NEt4]$^+$ cations were restrained to have similar geometries (SAME command in SHELXL, s.u. 0.02) and similar U parameters (SIMU command in SHELXL, s.u.0.01). The THF molecule was refined isotropically applying similar U parameter restraints (SIMU command in SHELXL, s.u. 0.01). Restraints to bond distances were applied as follows (s.u. 0.02): 1.47 Å for C−N and 1.53 Å for C−C in [NEt4]$^+$; 1.43 Å for C−O and 1.53 Å for C−C in THF. Since the crystals contain several strongly absorbing Pt atoms, high residual electron densities (ALERT A and B in CHECKCIF) remain after refinement close to the heavy atoms, in positions that are not realistic for any atom.

Table 5. Crystal Data and Experimental Details for $[NEt_4]_2[Pt_{33}(CO)_{38}]$·THF and $[NMe_3(CH_2Ph)]_5[NEt_4][Pt_{40}(CO)_{40}]$·3MeCN

	$[NEt_4]_2[Pt_{33}(CO)_{38}]$·THF	$[NMe_3(CH_2Ph)]_5[NEt_4][Pt_{40}(CO)_{40}]$·3MeCN
formula	$C_{58}H_{48}N_2O_{39}Pt_{33}$	$C_{104}H_{109}N_6O_{40}Pt_{40}$
Fw	7834.95	9928.60
T, K	100(2)	100(2)
λ, Å	0.71073	0.71073
crystal system	triclinic	triclinic
space group	P$\bar{1}$	P$\bar{1}$
a, Å	13.679(3)	15.778(2)
b, Å	14.772(3)	16.481(2)
c, Å	25.532(6)	28.555(4)
α, deg	106.077(2)	81.061(2)
β, deg	99.833(3)	81.175(2)
γ, deg	99.363(2)	89.248(2)
cell volume, Å^3	4762.9(18)(5)	7248.3(18)
Z	2	2
D_c, g cm^{-3}	5.463	4.549
μ, mm^{-1}	48.307	38.484
F(000)	6592	8472
crystal size, mm	0.16 × 0.13 × 0.11	0.16 × 0.12 × 0.11
θ limits, deg	1.45−25.03	1.25−27.00
index ranges	−16 ≤ h ≤ 16	−20 ≤ h ≤ 20
	−17 ≤ k ≤ 17	−21 ≤ k ≤ 21
	−30≤ l ≤ 30	−36≤ l ≤ 36
reflections collected	43041	80199
independent reflections	16 713 [R_{int} = 0.0847]	31 343 [R_{int} = 0.0656]
completeness to $θ_{max}$	99.2%	99.0%
data/restraints/parameters	16 713/726/1154	31 343/199/1738
goodness of fit on F^2	0.964	1.028
R_1 ($I > 2σ(I)$)	0.0557	0.0582
wR_2 (all data)	0.1423	0.1649
largest diff peak and hole, e Å^{-3}	3.981/−4.630	4.417/−2.803

[NMe3(CH2Ph)]5[NEt4][Pt40(CO)40]·3MeCN. The asymmetric unit of the unit cell contains one cluster anion, one [NEt4]$^+$ and five [NMe₃(CH₂Ph)]$^+$ cations and three MeCN molecules (all located on general positions). Some C and O atoms of the cluster anion and the cations have been restrained to isotropic behavior (ISOR command in SHELXL, s.u. 0.02). Since the crystals contain several strongly absorbing Pt atoms, high residual electron densities (ALERT A and B in CHECKCIF) remain after refinement close to the heavy atoms, in positions which are not realistic for any atom.

4.5. Electrochemical and Spectro-Electrochemical Measurements. Electrochemical measurements were recorded on a PrincetonApplied Research (PAR) 273A Potentiostat/Galvanostat, interfaced to a computer employing PAR M270 electrochemical software, and were performed in MeCN solutions containing [NnBu4][PF6] (0.1 mol dm^{-3}) as the supporting electrolyte at room temperature (20 ± 5 °C). High-performance liquid chromatography-grade MeCN (Sigma-Aldrich) was stored under argon over 3 Å molecular sieves. Electrochemical grade [NnBu4][PF6] was purchased from Fluka and used without further purification. Ferrocene (FeCp₂)[47] was prepared according to literature. Cyclic voltammetry was performed in a threeelectrode cell, having a platinum-disc working electrode, a platinum spiral counter electrode, and a quasi-reference electrode of platinum. After a sufficient number of voltammograms was recorded, a small amount of ferrocene was added to the solution, and a further voltammogram was recorded. Under the present experimental conditions, the one-electron oxidation of ferrocene occurs at E° = +0.39 V versus standard calomel electrode (SCE).

Infrared spectro-electrochemical measurements were performed using an OTTLE cell equipped with CaF₂ windows, platinum minigrid working and auxiliary electrodes, and silver wire pseudoreference electrode.[48] During the microelectrolysis procedures, the electrode potential was controlled by a Princeton Applied Research (PAR) 273A Potentiostat/Galvanostat, interfaced to a computer employing PAR M270 electrochemical software. Argon-saturated MeCN solutions of the compound under study, containing [NnBu4][PF6] 0.1 M as the supporting electrolyte, were used. The in situ spectro-electrochemical experiments were performed by collecting spectra of the solution at constant time intervals during the oxidation or reduction obtained by continuously increasing or lowering the initial working potential at a scan rate of 0.5 mV/s. IR spectra were recorded on a PerkinElmer FTIR 1725X spectro-photometer.

■ ASSOCIATED CONTENT

Supporting Information
Crystallographic data (CIF)
Crystallographic data (CIF)

View along (111) of $[Pt_{33}(CO)_{38}]^{2-}$ and its layers. IR spectra of $[Pt_{19}(CO)_{22}]^{4-}$, $[Pt_{19}(CO)_{22}]^{3-}$, and $[Pt_{40}(CO)_{40}]^{6-}$. Detailed sequences of the IR spectroelectrochemical studies of $[Pt_{33}(CO)_{38}]^{2-}$ and $[Pt_{40}(CO)_{40}]^{6-}$.

■ AUTHOR INFORMATION

Corresponding Authors
*E-mail: stefano.zacchini@unibo.it.
*E-mail: tiziana.funaioli@unipi.it.
Notes
The authors declare no competing financial interest.

■ ACKNOWLEDGMENTS

■ DEDICATION

We dedicate this paper to Prof. Giuliano Longoni in honor of his recent retirement from the Univ. of Bologna and in recognition of his fundamental contributions to metal carbonyl chemistry during the past 40 years.

■ REFERENCES

(1) (a) Chen, A.; Holt-Hindle, P. Chem. Rev. 2010, 110, 3767. (b) Ahmadi, T. S.; Wang, Z. L.; Green, T. C.; Henglein, A.; El-Sayed, M. A. Science 1996, 272, 1924.

(2) (a) Jin, R. Nanotechnol. Rev. 2012, 1, 31. (b) Bai, F.; Sun, Z.; Wu, H.; Haddad, R. E.; Xiao, X.; Fan, H. Nano Lett. 2011, 11, 3759. (c) Wang, J.; Zhang, X.-B.; Wang, Z.-L.; Wang, L.-M.; Xing, W.; Liu, X. Nanoscale 2012, 4, 1549.

(3) (a) Proch, S.; Wirth, M.; White, H. S.; Anderson, S. L. J. Am. Chem. Soc. 2013, 135, 3073. (b) Perez-Alonso, F. J.; McCarthy, D. N.; Nierhoff, A.; Hernandez-Fernandez, P.; Strebel, C.; Stephens, I. E. L.; Nielsen, J. H.; Chorkendorff, I. Angew. Chem., Int. Ed. 2012, 51, 4641.

(4) (a) Zhao, M. Q.; Crooks, R. M. Angew. Chem., Int. Ed. 1999, 38, 364. (b) Scheeren, C. W.; Machado, G.; Dupont, J.; Fichtner, P. F. P.; Texeira, S. R. Inorg. Chem. 2003, 42, 4738. (c) Mohanty, A.; Garg, N.; Jin, R. Angew. Chem., Int. Ed. 2010, 49, 4962.

(5) (a) Chen, G.; Yang, H.; Wu, B.; Zheng, Y.; Zheng, N. Dalton Trans. 2013, 42, 12699. (b) Stamenkovic, V. R.; Fowler, B.; Mun, B. S.; Wang, G.; Ross, P. N.; Lucas, C. A.; Markovic, N. M. Science 2007, 315, 493. (c) Yang, W.; Wang, X. L.; Yang, F.; Yang, C.; Yang, X. R. Adv. Mater. 2008, 20, 2579.

(6) (a) Alexeev, O. S.; Gates, B. C. Ind. Eng. Chem. Res. 2003, 42, 1571. (b) Liu, C.; Li, G.; Kauffman, D. R.; Pang, G.; Jin, R. J. Colloid Interface Sci. 2014, 423, 123. (c) Kawasaki, H.; Yamamoto, H.; Fujimori, H.; Arakawa, R.; Inada, M.; Iwasaki, Y. Chem. Commun. 2010, 46, 3759.

(7) (a) Imaoka, T.; Kitazawa, H.; Chun, W.-J.; Omura, S.; Albrecht, K. J. Am. Chem. Soc. 2013, 135, 13089. (b) Yamamoto, K.; Imaoka, T.; Chun, W.-J.; Enoki, O.; Katoh, H.; Takenaga, M.; Sonoi, A. Nat. Chem. 2009, 1, 397. (c) Imaoka, T.; Kitazawa, H.; Chun, W.-J.; Yamamoto, K. Angew. Chem., Int. Ed. 2015, 54, 9810.

(8) (a) Haruta, M. Catal. Today 1997, 36, 153. (b) Haruta, M. CATTECH 2002, 6, 102. (c) Kinayyigit, S.; Lara, P.; Lecante, P.; Philippot, K.; Chaudret, B. Nanoscale 2014, 6, 539.

(9) (a) Herzing, A. A.; Kiely, C. J.; Carley, A. F.; Landon, P.; Hutchings, G. J. Science 2008, 321, 1331. (b) Hutchings, G. J. Chem. Commun. 2008, 1148.

(10) (a) Li, G.; Jin, R. Acc. Chem. Res. 2013, 46, 1749. (b) Qian, H.; Zhu, M.; Wu, Z.; Jin, R. Acc. Chem. Res. 2012, 45, 1470. (c) Jin, R. Nanoscale 2010, 2, 343.

(11) Muetterties, E. L.; Rhodin, T. N.; Band, E.; Brucker, C. F.; Pretzer, W. R. Chem. Rev. 1979, 79, 91.

(12) (a) Harding, D. J.; Fielicke, A. Chem. - Eur. J. 2014, 20, 3258. (b) Catalytic Chemistry; Gates, B. C., Ed.; Wiley: New York, 1992.

(13) (a) Serna, P.; Gates, B. C. Acc. Chem. Res. 2014, 47, 2612. (b) Sun, Y.; Zhuang, L.; Lu, J.; Hong, X.; Liu, P. J. Am. Chem. Soc. 2007, 129, 15465.

(14) (a) Yang, Z.; Zhang, Y.; Wu, R. J. Phys. Chem. C 2012, 116, 13774. (b) Kim, H. Y.; Kim, D. H.; Ryu, J. H.; Lee, H. M. J. Phys. Chem. C 2009, 113, 15559. (c) Sun, Y.; Zhuang, L.; Lu, J.; Hong, X.; Liu, P. J. Am. Chem. Soc. 2007, 129, 15465.

(15) (a) Li, C.; Leong, W. K. J. Colloid Interface Sci. 2008, 328, 29. (b) Gutmann, T.; Walaszek, B.; Yeping, X.; Wächtler, M.; del Rosal, I.; Grünberg, A.; Poteau, R.; Axet, R.; Lavigne, G.; Chaudret, B.; Limbach, H.-H.; Buntkowsky, G. J. Am. Chem. Soc. 2010, 132, 11759. (c) Yamazoe, S.; Koyasu, K.; Tsukuda, T. Acc. Chem. Res. 2014, 47, 816.

(16) (a) Catalysis by Di- and Polynuclear Metal Cluster Complexes; Adams, R. D., Cotton, F. A., Eds.; Wiley-VCH: New York, 1998. (b) Metal Clusters in Chemistry; Braunstein, P., Oro, L. A., Raithby, P. R., Eds.; Wiley-VCH: Weinheim, Germany, 1999.

(17) (a) Clusters and Colloids; Schmid, G., Ed.; VCH: Weinheim, Germany, 1994. (b) Schmid, G.; Fenske, D. Philos. Trans. R. Soc., A 2010, 368, 1207. (c) Taketoshi, A.; Haruta, M. Chem. Lett. 2014, 43, 380.

(18) (a) Zacchini, S. Eur. J. Inorg. Chem. 2011, 2011, 4125. (b) Femoni, C.; Iapalucci, M. C.; Kaswalder, F.; Longoni, G.; Zacchini, S. Coord. Chem. Rev. 2006, 250, 1580.

(19) (a) Raithby, P. R. Platinum Metals Rev. 1998, 42, 146. (b) Johnson, B. F. G. Coord. Chem. Rev. 1999, 190−192, 1269. (c) Hogarth, G.; Kabir, S. E.; Nordlander, E. Dalton Trans. 2010, 39, 6153.

(20) (a) Lewis, G. J.; Roth, J. D.; Montag, R. A.; Safford, L. K.; Gao, X.; Chang, S.-C.; Dahl, L. F.; Weaver, M. J. J. Am. Chem. Soc. 1990, 112, 2831. (b) Roth, J. D.; Lewis, G. J.; Safford, L. K.; Jiang, X.; Dahl, L. F.; Weaver, M. J. J. Am. Chem. Soc. 1992, 114, 6159.

(21) Akdogan, Y.; Anantharaman, S.; Liu, X.; Lahiri, G. K.; Bertagnolli, H.; Roduner, E. J. Phys. Chem. C 2009, 113, 2352.

(22) Ciabatti, I.; Femoni, C.; Iapalucci, M. C.; Longoni, G.; Zacchini, S. J. Cluster Sci. 2014, 25, 115.

(23) (a) Femoni, C.; Kaswalder, F.; Iapalucci, M. C.; Longoni, G.; Mehlstäubl, M.; Zacchini, S. Chem. Commun. 2005, 5769. (b) Femoni, C.; Kaswalder, F.; Iapalucci, M. C.; Longoni, G.; Mehlstäubl, M.; Zacchini, S.; Ceriotti, A. Angew. Chem., Int. Ed. 2006, 45, 2060. (c) Femoni, C.; Iapalucci, M. C.; Longoni, G.; Lovato, T.; Stagni, S.; Zacchini, S. Inorg. Chem. 2010, 49, 5992.

(24) (a) Longoni, G.; Chini, P. J. Am. Chem. Soc. 1976, 98, 7225. (b) Calabrese, J. C.; Dahl, L. F.; Chini, P.; Longoni, G.; Martinengo, S. J. Am. Chem. Soc. 1974, 96, 2614.

(25) Fedi, S.; Zanello, P.; Laschi, F.; Ceriotti, A.; El Afefey, S. J. Solid State Electrochem. 2009, 13, 1497.

(26) (a) Chini, P. J. Organomet. Chem. 1980, 200, 37. (b) Ceriotti, A.; Masciocchi, N.; Macchi, P.; Longoni, G. Angew. Chem., Int. Ed. 1999, 38, 3724.

(27) Gao, F.; Li, C.; Heaton, B. T.; Zacchini, S.; Zarra, S.; Longoni, G.; Garland, M. Dalton Trans. 2011, 40, 5002.

(28) Washecheck, D. M.; Wucherer, E. J.; Dahl, L. F.; Ceriotti, A.; Longoni, G.; Manassero, M.; Sansoni, M.; Chini, P. J. Am. Chem. Soc. 1979, 101, 6110.

(29) (a) Ciabatti, I.; Femoni, C.; Iapalucci, M. C.; Longoni, G.; Zacchini, S.; Zarra, S. Nanoscale 2012, 4, 4166. (b) Femoni, C.; Iapalucci, M. C.; Longoni, G.; Zacchini, S.; Zarra, S. J. Am. Chem. Soc. 2011, 133, 2406.

(30) (a) Negishi, Y.; Nakazaki, T.; Malola, S.; Takano, S.; Niihori, Y.; Kurashige, W.; Yamazoe, S.; Tsukuda, T.; Häkkinen, H. J. Am. Chem. Soc. 2015, 137, 1206. (b) Zeng, C.; Qian, H.; Li, T.; Li, G.; Rosi, N. L.; Yoon, B.; Barnett, R. N.; Whetten, R. L.; Landman, U.; Jin, R. Angew. Chem., Int. Ed. 2012, 51, 13114. (c) Schnepf, A.; Schnöckel, H. Angew. Chem., Int. Ed. 2014, 53, 3064.

(31) (a) Liu, C.; Li, T.; Li, G.; Nobusada, K.; Zeng, C.; Pang, G.; Rosi, N. L.; Jin, R. Angew. Chem., Int. Ed. 2015, 54, 9826. (b) Shichibu, Y.; Zhang, M.; Kamei, Y.; Konishi, K. J. Am. Chem. Soc. 2014, 136, 12892. (c) Wan, X.-K.; Lin, Z.-W.; Wang, Q.-M. J. Am. Chem. Soc. 2012, 134, 14750.

(32) (a) Chen, J.; Zhang, Q.-F.; Bonaccorso, T. A.; Williard, P. G.; Wang, L.-S. J. Am. Chem. Soc. 2014, 136, 92. (b) Yang, H.; Wang, Y.; Yan, J.; Chen, X.; Zhang, X.; Häkkinen, H.; Zheng, N. J. Am. Chem. Soc. 2014, 136, 7197. (c) Das, A.; Li, T.; Nobusada, K.; Zeng, Q.; Rosi, N. L.; Jin, R. J. Am. Chem. Soc. 2012, 134, 20286.

(33) (a) Yang, H.; Wang, Y.; Lei, J.; Shi, L.; Wu, X.; Mäkinen, V.; Lin, S.; Tang, Z.; He, J.; Häkkinen, H.; Zheng, L.; Zheng, N. J. Am. Chem. Soc. 2013, 135, 9568. (b) Jin, R. Nanoscale 2015, 7, 1549. (c) Wan, X.- K.; Tang, Q.; Yuan, S.-F.; Jiang, D.-E.; Wang, Q.-M. J. Am. Chem. Soc. 2015, 137, 652.

(34) (a) Zhu, M.; Aikens, C. M.; Hollander, F. J.; Schatz, G. C.; Jin, R. J. Am. Chem. Soc. 2008, 130, 5883. (b) Heaven, M. W.; Dass, A.; White, P. S.; Holt, K. M.; Murray, R. W. J. Am. Chem. Soc. 2008, 130, 3754. (c) Qian, H.; Eckenhoff, W. T.; Zhu, Y.; Pintauer, T.; Jin, R. J. Am. Chem. Soc. 2010, 132, 8280.

(35) (a) Jadzinsky, P. D.; Calero, G.; Ackerson, C. J.; Bushnell, D. A.; Kornberg, R. D. Science 2007, 318, 430. (b) Femoni, C.; Iapalucci, M. C.; Longoni, G.; Tiozzo, C.; Zacchini, S. Angew. Chem., Int. Ed. 2008, 47, 6666.

(36) (a) Cordero, B.; Gómez, V.; Platero-Prats, A. E.; Revés, M.; Echeverría, J.; Cremades, E.; Barragán, F.; Alvarez, S. Dalton Trans. 2008, 2832. (b) Bondi, A. J. Phys. Chem. 1964, 68, 441.

(37) (a) Vidal, J. L.; Schoening, R. C.; Troup, J. M. Inorg. Chem. 1981, 20, 227. (b) Collini, D.; Fabrizi De Biani, F.; Dolzhnikov, D. S.; Femoni, C.; Iapalucci, M. C.; Longoni, G.; Tiozzo, C.; Zacchini, S.; Zanello, P. Inorg. Chem. 2011, 50, 2790.

(38) Fumagalli, A.; Martinengo, S.; Ciani, G.; Masciocchi, N.; Sironi, A. Inorg. Chem. 1992, 31, 336.

(39) (a) Mednikov, E. G. Russ. Chem. Bull. 1993, 42, 1242. (b) Mednikov, E. G.; Dahl, L. F. Philos. Trans. R. Soc., A 2010, 368, 1301.

(40) Johnson, W. N. Can. J. Math. 1966, 18, 169.

(41) Zanello, P. Inorganic Electrochemistry. Theory, Practice and Application; RSC: Cambridge, U.K., 2003.

(42) Ragaini, F.; Song, J.-S.; Ramage, D. L.; Geoffroy, G. L.; Yap, G. A. P.; Rheingold, A. L. Organometallics 1995, 14, 387.

(43) Longoni, G.; Femoni, C.; Iapalucci, M. C.; Zanello, P. In Metal Clusters in Chemistry; Braunstein, P., Oro, L. A., Raithby, P. R., Eds.; Wiley-VCH: New York, 1999; pp 1137−1158.

(44) Keller, E. SCHAKAL99; University of Freiburg: Germany, 1999.

(45) Sheldrick, G. M. SADABS, Program for empirical absorption correction; University of Göttingen: Germany, 1996.

(46) Sheldrick, G. M. SHELX97, Program for crystal structure determination; University of Göttingen: Germany, 1997.

(47) Wilkinson, G. Org. Synth. 1956, 36, 31.

(48) Krejčik, M.; Daněk, M.; Hartl, F. J. Electroanal. Chem. Interfacial Electrochem. 1991, 317, 179.